A Camera-based Optical Calibration System for Water-based Neutrino Telescopes

Wei Tian,[a,*] **Wei Zhi**[b] **and Donglian Xu**[a,b] **for the TRIDENT collaboration**

[a]*Tsung-Dao Lee Institute, Shanghai Jiao Tong University, Shanghai 201210, China*

[b]*School of Physics and Astronomy, Shanghai Jiao Tong University, Key Laboratory for Particle Astrophysics and Cosmology (MoE), Shanghai Key Laboratory for Particle Physics and Cosmology, Shanghai 200240, China*

E-mail: tianwei1997@sjtu.edu.cn

The angular resolution and energy threshold of a water-based neutrino telescope are significantly influenced by the level of absorption and scattering experienced by Cherenkov photons in the medium. Unlike glacial ice, the dynamic water environment can lead to changing optical properties within the large detector volume. Therefore, the use of a real-time calibration system among the detector array is necessary. This paper introduces a novel calibration system based on CMOS cameras and steady LED light sources. Its efficient image processing algorithms enable real-time optical measurements. The system is highly suitable for implementation in the future TRIDENT detector. The successful demonstration of this camera system at a depth of 3420m by the T-REX experiment in 2021 further validates its effectiveness.

ICRC2023
38th International Cosmic Ray Conference
The Astroparticle Physics Conference

---

*Speaker

1. Introduction

The Tropical Deep-sea Neutrino Telescope (TRIDENT) [1] is a planned multi-cubic-kilometer neutrino telescope in the Western Pacific Ocean, with a proposed detection volume of 7.5 km^3 at a depth of 3500 meters. TRIDENT aims to enhance the search for high-energy neutrino sources and all-flavor neutrino detection, building on the success of IceCube's observations [2–6], while also providing complementary neutrino sky observations due to its equatorial location. The TRIDENT Pathfinder experiment (TRIDENT Explorer, T-REX for short), conducted in 2021, focused on measuring in-situ optical properties and radioactivity of the deep-sea water at a depth of 3420 meters.

Neutrino telescopes detect high-energy neutrinos by observing Cherenkov radiation in a transparent medium like water or glacial ice. Therefore, random absorption and scattering of photons during propagation in the medium directly impact the telescope's performance, affecting angular resolution and energy threshold. Real-time optical calibration becomes crucial to address these effects and ensure accurate event reconstruction across the detector array, especially for a fluid water-based neutrino telescope. Existing neutrino telescopes have utilized various calibration techniques, including Photon Multiplier Tubes (PMTs) assisted by pulsing light sources [7–9], as well as commercial or custom laser apparatus [10, 11]. These methods usually require precise time synchronization or face challenges in achieving real-time calibration over a large detector volume.

As a well-established technology, micro CMOS cameras offer significant potential for optical calibration in neutrino telescopes. They can be easily integrated into digital optical modules, providing comprehensive calibration coverage. Ongoing research explores the use of CMOS cameras for bioluminescence monitoring and scattering calibration in glacial ice [12–14]. In this paper, we present an in-situ calibration system based on CMOS cameras, successfully demonstrated by the T-REX experiment at a depth of 3420 meters. The system is designed for optical properties measurement and environmental monitoring.

2. Hardware of the camera system

The T-REX apparatus consists of a light emission module (LEM) and two light receiver modules (LRM), LRM-A and LRM-B. LRM-A is positioned at a vertical distance of 21.73 ± 0.02 m from the LEM, while LRM-B is located at 41.79 ± 0.04 m, as illustrated in Figure 1. Each LRM is equipped with a CMOS camera (Cam-A or Cam-B) and three 3-inch PMTs, capable of detecting light signals from the central LEM at two different distances. The LEM has two emission modes: steady mode and pulsing mode. The steady mode employs LEDs with three different wavelengths (405 nm, 460 nm, and 525 nm) to provide a constant and consistent illumination for capturing clear images. The pulsing mode is designed for PMT system.

The camera system consists of a monochromatic 5M-pixel camera with a 25mm-focal-length lens, offering a viewing angle of approximately 16° in water. It is controlled by a Raspberry Pi module, which provides power and enable the real-time data transmission back to the research vessel's during the deployment. The Raspberry Pi module is also equipped with temperature-humidity and acceleration-rotation sensors to record the internal environment and dynamic state of the LRM in real-time.
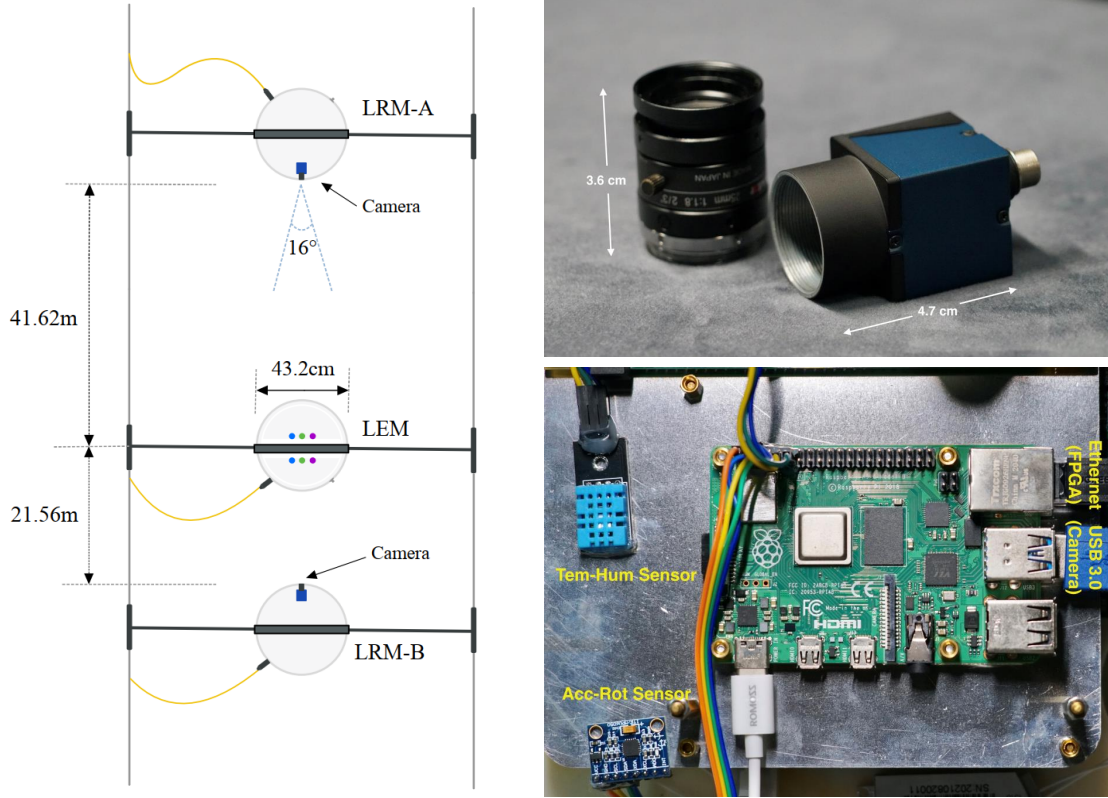
Figure 1: An illustration of experimental set-up of the T-REX

To accommodate varying underwater conditions and light intensities of the LEM at different wavelengths, the camera system is configured with a range of exposure times and gains. This ensures that the gray values in the captured images remain within the linear response range for subsequent image processing. For each combination of exposure time and gain, the camera captures 20 images in a repeated manner.

3. I_{center} method for attenuation measurement

In this study, we propose two measurement methods based on light propagation models to determine optical parameters using images captured by the cameras of the LRMs. These cameras record both direct and scattered photons from the steady LEM.

The first method is the I_{center} method, which allows for a quick measurement of the canonical attenuation length. In the T-REX experiment, each camera within the LRMs can be treated as a pinhole camera due to its long distance from the LEM. Each pixel records the light intensity within a unit solid angle from a specific direction, converting it into a gray value. Since the viewing angles occupied by the LEM are small (approximately $0.6°$ for Cam-A and $1.1°$ for Cam-B), the directly-arrived photons from the LEM are highly collimated, while the scattered photons have a wider angular distribution. By considering only the light intensity within a unit viewing angle

centered on the pixel, we can effectively exclude most of the scattered photons. From Equation **??**, we obtain:

$$\lambda_{\text{att}} = -(L_A - L_B)/\ln\left(-\frac{I_A}{I_B} \cdot \frac{I_0'}{I_0}\right) \tag{1}$$

Here, I_A and I_B represent the mean gray values of the center pixels of the LEM recorded by Cam-A and Cam-B, respectively, with the same exposure time and gain. L_A and L_B are the respective measurement distances from the LEM, and $L_A \approx 2L_B$, as illustrated in Figure **??**. The imperfections of the LEM are taken into account by expressing the initial light intensity ratio of the two sides of the LEM in terms of I_0/I_0', which is well-calibrated in our laboratory.

To address uncertainties caused by scattered photons with very small scattering angles or photons from other initial directions entering this viewing angle, we conducted a detailed Geant4 simulation. Through the analysis of simulation data using the I_{center} method, we confirmed that the potential measurement bias is less than 4%, even under extreme conditions where the scattering length is less than 30 m [15].
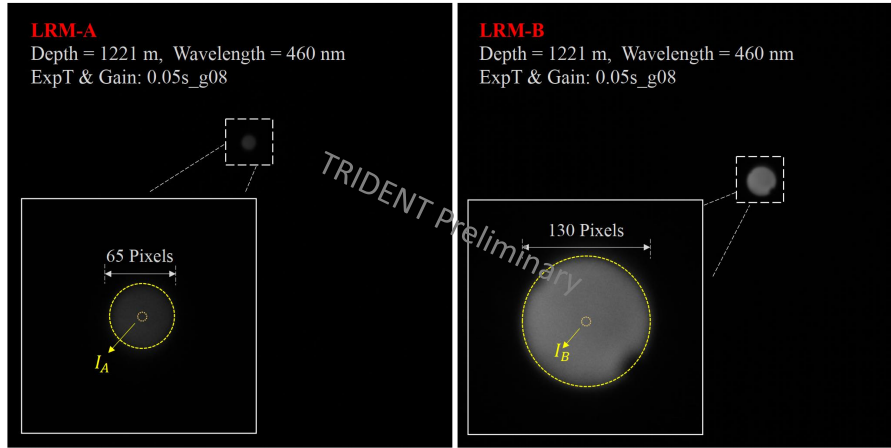
Figure 2: An illustration of image processing. The dashed yellow circle indicates the profile of the LEM on each images. The central region is selected fro calculating the mean gray value of the centroid pixel.

For image processing in the I_{center} method, we select images where each pixel is unsaturated, typically with gray values between 20-230 for our 8-bit cameras. Then, we crop the image around the gray value centroid of the LEM, resulting in a 300×300 pixel size, as shown in Figure 2. This cropping process allows for accurate positioning of the LEM in a series of images taken with the same camera settings and prepares the image for subsequent stacking to reduce statistical uncertainties. Next, we employ a fitting method to extract the background from outer region of each image, where the image records both scattered light and intrinsic noise of the CMOS sensor. We then compute the mean gray value of 100 pixels around the centroid and subtract the background contribution to obtain I_A and I_B, which are used to calculate the attenuation length λ_{att}.

Using this relative measurement method offers several advantages. It can eliminate some systematic uncertainties that commonly affect the two LRMs, such as light loss at the glass shell interfaces and the effects of low temperatures in deep-sea environments. Furthermore, this efficient

algorithm allows for real-time optical calibration, as the attenuation length can be calculated even with two images captured by Cam-A and Cam-B.

3.1 Statistical χ^2 test for λ_{abs} and λ_{sca} measurement

We developed a statistical χ^2 model to extract λ_{abs} and λ_{sca} from the measured λ_{att}. We used Geant4 to generate a comprehensive simulation dataset, exploring the phase space of λ_{abs}, λ_{sca}, $\langle\cos\theta\rangle$, and refractive index for all three wavelengths.

For real image processing, we applied the same pre-processing steps as in the I_{center} method. We converted the 2D images into 1D gray value distribution profiles and applied a joint normalization to both Cam-A and Cam-B data to preserve the initial gray value ratio. In the simulation data processing, we incorporated the calibrated response characteristics of the cameras and the LEM [16]. We re-weighted the emitted photons from the isotropic light source based on a pre-calibrated profile of the LEM's nonuniformity. Additionally, we accounted for the potential defocusing effect of the cameras using a 2D-Gaussian Point Spread Function (PSF) with the PSF parameter treated as a nuisance parameter.

Using the χ^2 model, we calculated the χ^2 value bin by bin to compare the normalized mean gray values of the real images (M_i) with the simulated values (T_i). Nuisance parameters (ϵ_k) were included to account for uncorrelated systematic uncertainties.

$$\chi^2 = \sum_{i=1}^{N} \frac{[M_i - T_i(1 + \sum_{k=1}^{K} \epsilon_k)]^2}{\sigma_{Mi}^2 + \sigma_{Ti}^2} + \sum_{k=1}^{K} \frac{\epsilon_k^2}{\sigma_k^2}. \tag{2}$$

By minimizing the χ^2 across the simulation phase space, we obtained the values of λ_{abs} and λ_{sca}. However, differentiating between Mie and Rayleigh scattering from the overall effect of λ_{sca} remains challenging. We are developing a more detailed algorithm to distinguish between them, which involves fitting the full image area, including the weak scattering light.
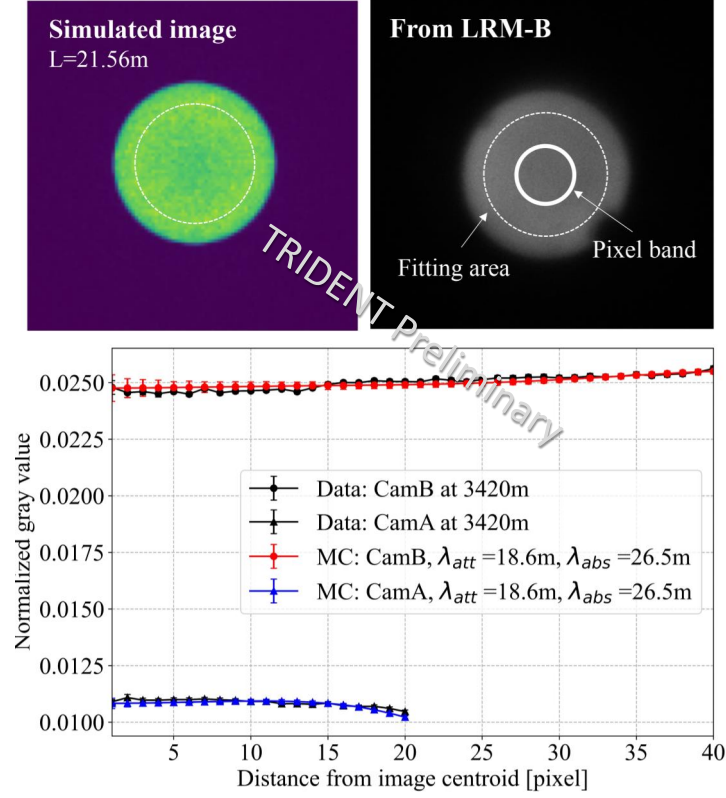
Figure 3 shows the best-fitted optical parameters for data recorded at 3420 m with minimum χ^2. The black points represent data from real images, while the red and blue points represent simulation results. The algorithm's development to differentiate between Mie and Rayleigh scattering is ongoing.

4. Calibration of the camera system

4.1 Linear Response Calibration

To verify the linear response of the CMOS sensor, we conducted experiments using a steady light source in a darkroom. Since the exposure time was directly proportional to the captured photon number, we measured the gray values of identical pixels in the images with different exposure times while keeping the gain constant.

The test results confirmed a constant stable linear response within the operating range of the cameras. The gray value in the image are proportional to the photon number very well.

Figure 3: Upper: An illustration of image processing of simulated and real images in statistical χ^2 analysis. Lower: The best-fitted optical parameters for data recorded at 3420 m with minimum χ^2. The black points represent data from real images, while the red and blue points correspond to simulated data.

4.2 Low-Temperature Calibration

To ensure the capability in deep-sea temperature, which is $2 \sim 4°C$ specifically, we conducted temperature-controlled experiments to calibrate the camera system, the Light Emission Module (LEM) and their control system. We measured I_0'/I_0 at the two temperatures, $2.1 \pm 0.5°C$ and $18.9 \pm 0.5°C$ respectively. And the measurement for all three wavelengths are conducted. The results revealed that the low-temperature effect on the system performance was negligible, with an influence of less than 1%.

Additionally, we calibrated the LEM's light emission profile, which accounts for the non-uniformity of light intensity emitted from different latitudes in both hemispheres. This calibration step further ensured reliable image processing and accurate data interpretation in χ^2 analysis.

4.3 Long-Distance Test in Air

We conducted tests in a dark room with varying distances to verify the suitability of viewing angle for long-distance measurements in the deep sea. The goal was to determine the camera's performance in capturing clear and undistorted images over long distances. The images were analyzed using the Hough-Circle algorithm and the results show that the radius of the LEM in the

images consistently followed a $1/L$ decrease as the distance changed. This confirmed the validity of the pin-hole camera model assumption and indicated that the camera system could accurately capture long-distance images without significant distortion. The results provided confidence in the camera's performance for deep-sea imaging applications.

4.4 Water Tank Experiment

To evaluate the camera system's sensitivity to the attenuation effect in water, we conducted a scaled-down water tank experiment. The effectiveness of the I_{center} method was confirmed by comparing the results obtained in air and tap water.

A stainless steel water tank with a flanged window and guide rails with a length of 320 ± 1 cm was used for the experiment. The flanged window incorporated an organic glass window to accommodate the camera and isolate it from the water. The guide rails facilitated the movement of a light source platform along the rails, allowing precise distance adjustments.

This water tank experiment not only validated the reliability of the I_{center} method for attenuation measurements in water but also established the potential of the water tank as a valuable calibration facility for future applications.

4.5 Focal Length Re-calibration in Water

To account for the potential influence of the glass shell's curvature and the refractive index difference between the inside and outside of the shell, we conducted experiments in a large ship towing tank to recalibrate the focal length of our cameras for underwater imaging.

A 15 cm-diameter waterproof light source was positioned at the bottom of the tank with the depth of 7.5 m, and the camera captured images through the glass shell on the water surface. By adjusting the camera's focal length in this setup, we aimed to ensure clear image recording under underwater conditions. This setup allowed us to simulate underwater imaging conditions and adjust the camera's focal length accordingly. The optimal image quality for underwater imaging during the deep-sea experiment can be ensured.

5. Summary and outlook

In conclusion, we have presented a compact camera system for optical calibration in water-based neutrino telescopes, successfully demonstrated in TRIDENT's pathfinder experiment.

We introduced two analysis methods: the I_{center} method for measuring the attenuation length and the statistical χ^2 test for decoding absorption and scattering lengths. Extensive laboratory calibration accounted for potential influences on the camera system's performance.

The camera system's efficient data transmission and quick analysis algorithm make it suitable for real-time optical calibration in future experiments. However, further optimization is still required for future application in the TRIDENT detector. With ongoing improvements, this camera system holds promise for enhancing neutrino research and detection capabilities.

References

[1] Z. P. Ye *et al.*, "Proposal for a neutrino telescope in South China Sea," 7 2022.

[2] F. Halzen and S. R. Klein, "IceCube: An Instrument for Neutrino Astronomy," *Rev. Sci. Instrum.*, vol. 81, p. 081101, 2010.

[3] M. G. Aartsen *et al.*, "Neutrino emission from the direction of the blazar TXS 0506+056 prior to the IceCube-170922A alert," *Science*, vol. 361, no. 6398, pp. 147–151, 2018.

[4] R. Abbasi *et al.*, "Evidence for neutrino emission from the nearby active galaxy NGC 1068," *Science*, vol. 378, no. 6619, pp. 538–543, 2022.

[5] N. Song, S. W. Li, C. A. Argüelles, M. Bustamante, and A. C. Vincent, "The Future of High-Energy Astrophysical Neutrino Flavor Measurements," *JCAP*, vol. 04, p. 054, 2021.

[6] R. Abbasi *et al.*, "Search for quantum gravity using astrophysical neutrino flavour with Ice-Cube," *Nature Phys.*, vol. 18, no. 11, pp. 1287–1292, 2022.

[7] J. A. Aguilar *et al.*, "Transmission of light in deep sea water at the site of the ANTARES Neutrino Telescope," *Astropart. Phys.*, vol. 23, pp. 131–155, 2005.

[8] N. Bailly *et al.*, "Two-year optical site characterization for the Pacific Ocean Neutrino Experiment (P-ONE) in the Cascadia Basin," *Eur. Phys. J. C*, vol. 81, no. 12, p. 1071, 2021.

[9] E. G. Anassontzis *et al.*, "Light transmission measurements with LAMS in the Mediterranean Sea," *Nucl. Instrum. Meth. A*, vol. 626-627, pp. S120–S123, 2011.

[10] A. Capone *et al.*, "Measurements of light transmission in deep sea with the AC9 transmissometer," *Nucl. Instrum. Meth. A*, vol. 487, pp. 423–434, 2002.

[11] E. V. Rjabov and B. Tarashansky, "Monitoring of optical properties of deep lake water," *PoS*, vol. ICRC2021, p. 1034, 2021.

[12] R. Barbier, "Biocam in km3net and antares," Camera-systems and image analysis for neutrino detectors calibration, glaciology and deep sea exploration, Online Workshop, 2021.

[13] I. C. Rea *et al.*, "P-ONE second pathfinder mission: STRAW-b," *PoS*, vol. ICRC2021, p. 1092, 2021.

[14] R. Abbasi *et al.*, "Camera Calibration for the IceCube Upgrade and Gen2," *PoS*, vol. ICRC2021, p. 1064, 2021.

[15] F. Hu *et al.*, "Simulation study on the optical processes at deep-sea neutrino telescope sites," 2 2023.

[16] W. Li *et al.*, "The Light Source of the TRIDENT Pathfinder Experiment," 4 2023.

PoS(ICRC2023)1094